

# A Method for Diagnosing the Sources of Infrasound in Convective Storm Simulations

DAVID A. SCHECTER

*NorthWest Research Associates, Redmond, Washington*

(Manuscript received 5 January 2011, in final form 8 July 2011)

## ABSTRACT

This paper presents a convenient method for diagnosing the sources of infrasound in a numerical simulation of a convective storm. The method is based on an exact acoustic wave equation for the perturbation Exner function  $\Pi'$ . One notable source term ( $S_{uu}$ ) in the  $\Pi'$  equation is commonly associated with adiabatic vortex fluctuations, whereas another ( $S_m$ ) is directly connected to the heat and mass generated or removed during phase transitions of moisture. Scale estimates suggest that other potential sources are usually unimportant. Simple numerical simulations of a disturbed vortex and evaporating cloud droplets are carried out to illustrate the infrasound of  $S_{uu}$  and  $S_m$ . Moreover, the diagnostic method is applied to a towering cumulonimbus simulation that incorporates multiple categories of ice, liquid, and mixed-phase hydrometeors. The sensitivity of  $S_m$  to the modeling of the hail-to-rain category conversion is briefly addressed.

## 1. Introduction

The term “infrasound” refers to acoustic waves with frequencies that are less than the lower limit of unimpaired human hearing (20 Hz). There are many natural sources of infrasound, including avalanches, volcanoes, ocean waves, and severe weather (e.g. Bedard and Georges 2000; Johnson et al. 2004; Waxler and Gilbert 2006; Bedard 2005). Here we are concerned with the last of these. Observational studies have shown that severe storms can emit abnormally strong, sustained infrasound in the 0.5–5-Hz frequency range (Bedard 2005; Bedard et al. 2004; Szoke et al. 2004; Passner and Noble 2006). Bedard (2005) summarizes the evidence suggesting that the infrasonic emissions come from developing and mature tornadoes. However, some ambiguity remains in the interpretation of the data. It is fair to say that we do not yet fully understand the conditions for which a vortex signal is discernible from the infrasound of nontornadic sources within a storm. There is a pressing need to advance our fundamental understanding of the different mechanisms that generate infrasound in atmospheric convection.

To gain further insight, numerical modeling may be the best method of investigation. This avenue of research

is being explored with a version of the Regional Atmospheric Modeling System (c-RAMS) that has been customized to simulate acoustic phenomena (Nicholls and Pielke 1994a,b, 2000; Cotton et al. 2003). By comparison with analytical results, it has been shown that c-RAMS adequately generates the infrasound of tornado-like vortices and of simple diabatic cloud processes such as droplet evaporation (Schechter et al. 2008, hereinafter S08; Schechter and Nicholls 2010, hereinafter SN10). The basic credibility of the model justifies pushing ahead (cautiously) with simulations of infrasound generated by realistic convective systems. The main purpose of this paper is to expound a general method for diagnosing the primary sources of infrasound in complex storm simulations.

An acoustic source is rigorously defined as a term on the right-hand side of an inhomogeneous acoustic wave equation (AWE). An exact AWE of the form

$$\mathcal{L}_{fw}(\mathcal{A}) = \sum_{\alpha} \mathcal{S}_{\alpha} \quad (1)$$

can always be derived from the primitive fluid equations (e.g. Lighthill 1952; Stein 1967; Aurégan et al. 2002; Goldstein 1976, 2003; Howe 2003; Akhalkatsi and Gogoberidze 2009). The result is said to form the basis of an “acoustic analogy.” Here,  $\mathcal{A}$  is a select acoustic variable, such as the pressure or density perturbation, and  $\mathcal{L}_{fw}$  is the free-wave operator for  $\mathcal{A}$  that is known from sound propagation theory. In general, the source term  $\mathcal{S}_{\alpha}$  is a function of one or more fluid variables that

*Corresponding author address:* David A. Schechter, NorthWest Research Associates, CoRA Division, 3380 Mitchell Lane, Boulder, CO 80301.

E-mail: [schechter@nwra.com](mailto:schechter@nwra.com)

becomes negligible in the radiation zone. In the ideal case, each source term is readily associated with a well-defined physical mechanism of sound generation, such as a vortex fluctuation or phase transition of moisture.

Lighthill (1952, 1954) first derived an AWE for the density perturbation and showed that homentropic turbulence at low Mach number acts as a weak quadrupole source of acoustic radiation. A more recent approach, advocated by Howe, uses total enthalpy as the acoustic variable  $\mathcal{A}$  (e.g. Howe 2003). Working in this modern framework, Akhalkatsi and Gogoberidze (2009, 2011, hereinafter AG09 and AG11, respectively) showed that phase transitions of moisture in vigorous cloud turbulence could theoretically dominate the production of 0.1–1-Hz infrasound in a severe storm. The approach taken here is to let  $\mathcal{A}$  equal the perturbation Exner function, which is a traditional surrogate for the pressure perturbation in cloud models. This choice seems equally (or more) convenient for analyzing the acoustic sources in a c-RAMS simulation, and it facilitates a succinct discussion of an acoustic source that c-RAMS tacitly neglects.

Part of this paper will address the physical meaning of the primary acoustic sources that appear in the Exner function formalism. Scale analyses will establish the subdominance of other sources under ordinary circumstances. Moreover, this paper will demonstrate how to find the prevailing source of infrasound in a complex storm simulation when the answer is not entirely clear.

The remaining sections are organized as follows: section 2 derives the AWE for the perturbation Exner function and discusses the significance of each source term. Section 3 describes the computational procedure that is used to obtain the infrasonic radiation field of a given source. Section 4 validates the procedure by successfully comparing its results with the infrasound generated in two benchmark c-RAMS simulations. Section 5 illustrates how to establish the prevailing source in a complex storm simulation by analyzing the production of infrasound in a towering cumulonimbus. Section 6 summarizes the principal findings of this paper.

## 2. The acoustic analogy

### a. Simple derivation of the acoustic analogy

In c-RAMS, the Cartesian components of the velocity field  $\{u_i\}$  are governed by

$$\begin{aligned} \partial_t u_i = & -u_j \partial_j u_i - \theta_{v0} \partial_i \Pi' + g \left[ \frac{\theta'_v}{\theta_{v0}} - (r_t - r_v) \right] \delta_{i3} \\ & + \varepsilon_{ij3} f u_j + \partial_j \sigma_{ij}, \end{aligned} \quad (2)$$

in which  $\Pi \equiv c_p(p/p_a)^{R/c_p}$  is the Exner function,  $\theta_v \equiv c_p p / R \rho \Pi$  is the virtual potential temperature,  $r_t$  is the

total water mixing ratio,  $r_v$  is the vapor mixing ratio,  $g$  is gravitational acceleration,  $f$  is the Coriolis parameter, and  $\sigma_{ij}$  is the viscous stress tensor associated with small-scale turbulence. In the definitions of  $\Pi$  and  $\theta_v$ ,  $p$  is total pressure,  $p_a = 10^5$  Pa, and  $\rho$  is the mass density of the gaseous component of moist air. The parameters  $c_p$ ,  $c_v$  (used later), and  $R$  denote the specific heat at constant pressure, the specific heat at constant volume, and the gas constant of dry air. The symbols  $\partial_t$  and  $\partial_i$  denote partial derivatives with respect to time  $t$  and the Cartesian coordinate  $x_i$ . The symbols  $\delta_{ij}$  and  $\varepsilon_{ijk}$  represent the Kronecker-delta and Levi-Civita tensors, respectively. A zero subscript or prime denotes an ambient or perturbation field. Here it is assumed that the basic state is at rest and that the ambient fields depend only on the vertical coordinate  $x_3$ . The Einstein convention is used here and throughout this paper, such that repeated indices ( $i$  or  $j$ ) in a given product are summed over all possible values  $\{1, 2, 3\}$ . Note that the right-hand side of Eq. (2) neglects the term  $-\theta'_v \partial_i \Pi'$ , under the assumption that it is subdominant with respect to  $-\theta_{v0} \partial_i \Pi'$ . Section 2h briefly addresses the consequences of this approximation on the production of infrasound.

Also in c-RAMS, the perturbation Exner function is governed by

$$\begin{aligned} \partial_t \Pi' + \frac{c_0^2}{\rho_0 \theta_{v0}^2} \partial_i (\rho_0 \theta_{v0} u_i) = & -u_i \partial_i \Pi' - \frac{R}{c_v} \Pi' \partial_i u_i + \frac{c^2}{\theta_v^2} \frac{d\theta_v}{dt} \\ & + \frac{c^2}{\theta_v (1 + r_v)} \frac{dr_v}{dt}, \end{aligned} \quad (3)$$

in which  $c^2 \equiv R \Pi \theta_v / c_v$  is the square of the nominal sound speed and  $d/dt \equiv \partial_t + u_i \partial_i$ . Equation (3) is readily derived by combining

$$\frac{d}{dt} \left( \frac{\Pi}{c_p} \right)^{c_v/R} \equiv \frac{R}{p_a} \frac{d}{dt} (\rho \theta_v) \quad (4)$$

with the mass continuity equation,

$$\frac{d\rho}{dt} = -\rho \partial_i u_i + \frac{\rho}{1 + r_v} \frac{dr_v}{dt}. \quad (5)$$

Because the derivation is straightforward, further elaboration seems unnecessary.

Substituting the right-hand side of Eq. (2) for  $\partial_t u_i$  into the left-hand side of  $\partial_t \Pi'$  [Eq. (3)] yields the following AWE:

$$\begin{aligned} \partial_{tt} \Pi' - \frac{c_0^2}{\rho_0 \theta_{v0}^2} \partial_i (\rho_0 \theta_{v0}^2 \partial_i \Pi') = & S_m + S_{uu} + S_{pu} \\ & + S_b + S_c + S_{tb}, \end{aligned} \quad (6)$$

in which

$$\begin{aligned}
 S_m &\equiv \partial_t \left[ \frac{c^2}{\theta_v^2} \frac{d\theta_v}{dt} + \frac{c^2}{\theta_v(1+r_v)} \frac{dr_v}{dt} \right], \\
 S_{uu} &\equiv \frac{c_0^2}{\rho_0 \theta_{v0}^2} \partial_i (\rho_0 \theta_{v0} u_j \partial_j u_i), \\
 S_{pu} &\equiv -\partial_t \left( u_i \partial_i \Pi' + \frac{R}{c_v} \Pi' \partial_i u_i \right), \\
 S_b &\equiv -\frac{c_0^2}{\rho_0 \theta_{v0}^2} \partial_3 \{ g \rho_0 [\theta'_v - \theta_{v0}(r_t - r_v)] \}, \\
 S_c &\equiv -\frac{c_0^2}{\theta_{v0}} \partial_i (\varepsilon_{ij3} f u_j), \\
 S_{tb} &\equiv -\frac{c_0^2}{\rho_0 \theta_{v0}^2} \partial_i (\rho_0 \theta_{v0} \partial_j \sigma_{ij}), \quad (7)
 \end{aligned}$$

and  $\partial_{tt}$  is the second-order time derivative. Equation (6) forms the basis of the acoustic analogy. Relating Eq. (6) to Eq. (1) gives

$$\mathcal{L}_{fw} = \partial_{tt} - \frac{c_0^2}{\rho_0 \theta_{v0}^2} \partial_i (\rho_0 \theta_{v0}^2 \partial_i)$$

and  $\mathcal{A} = \Pi'$ . It is asserted that each term on the right-hand side of Eq. (6) is negligible in the radiation zone (when compared with terms on the left-hand side) and therefore qualifies as a legitimate acoustic source. Most source terms are negligible in the radiation zone because they are quadratic in the perturbation fields. The linear terms are relatively small (outside the storm) for reasons given below.

In what follows, the significance of each source term that appears in the acoustic analogy is discussed. The terms  $S_m$  and  $S_{uu}$  are considered first, because they are thought to be the primary source candidates in convective storm simulations. Scale estimates are generally required to demonstrate the subdominance of all other source terms. To limit distraction, the more involved estimates are set aside in appendix A.

*b. The source term associated with phase transitions of moisture:  $S_m$*

The source term  $S_m$  is directly connected to heat and mass production by phase transitions of moisture. It is linear to lowest order but vanishes in the radiation zone, which is assumed to be unsaturated and devoid of hydrometeors. As mentioned earlier, theoretical studies suggest that  $S_m$  in moist turbulence may contribute

significantly to the infrasound of a severe storm at frequencies of order 0.1–1 Hz (AG09; AG11; SN10). Whether this contribution prevails over tornado emissions in a credible supercell simulation remains to be seen.

*c. The source term associated with vortices and turbulence:  $S_{uu}$*

The source term  $S_{uu}$  is commonly associated with adiabatic vortex fluctuations or turbulence. It is readily expanded as follows:

$$\begin{aligned}
 \frac{c_0^2}{\rho_0 \theta_{v0}^2} \partial_i (\rho_0 \theta_{v0} u_j \partial_j u_i) &\equiv \frac{c_0^2}{\theta_{v0}} \nabla \cdot (\boldsymbol{\zeta} \times \mathbf{u}) + \frac{c_0^2}{2\theta_{v0}} \nabla^2 \mathbf{u}^2 \\
 &\quad + \frac{c_0^2}{\theta_{v0}} \partial_3 [\ln(\rho_0 \theta_{v0})] u_j \partial_j u_3, \quad (8)
 \end{aligned}$$

in which  $\nabla \equiv \hat{x}_i \partial_i$  is the gradient operator,  $\mathbf{u} \equiv \hat{x}_i u_i$  is the velocity vector, and  $\boldsymbol{\zeta} \equiv \nabla \times \mathbf{u}$  is the vorticity vector. In classic vortex sound theory (Powell 1964; Howe 2003), the far-field acoustic radiation of the explicit vorticity term  $c_0^2 \theta_{v0}^{-1} \nabla \cdot (\boldsymbol{\zeta} \times \mathbf{u})$  dominates that of all other terms on the right-hand side of Eq. (8). The classic theory assumes low Mach number, an acoustically compact vorticity field, and insignificant ambient stratification. Of course, strong tornadoes can have Mach numbers approaching one-half (0.4) and radial length scales greater than the infrasonic wavelengths of interest. This alone suggests that classic vortex sound theory might not always provide an accurate description of tornado emissions, regardless of any diabatic processes that it neglects.

*d. The mixed pressure–velocity source:  $S_{pu}$*

At first glance, the significance of  $S_{pu}$  is not entirely obvious. In practice, it is found that the acoustic radiation field of  $S_{pu}$  is generally subdominant to other contributions. Appendix A provides theoretical explanations for this observation, in the context of two standard paradigms. The first paradigm involves the infrasound of dry-adiabatic turbulence, whereas the second paradigm involves the infrasound of an evaporating cloud of water droplets.

*e. The buoyancy source:  $S_b$*

The source term proportional to the vertical gradient of the buoyancy acceleration ( $S_b$ ) is linear. For the study of gravity waves,  $S_b$  cannot be neglected in the radiation zone (e.g., Stein 1967). However, the acoustic waves of interest are characterized by the condition  $\omega \gg N$ , in which  $\omega$  is the wave frequency and

$$N \equiv \sqrt{g \partial_3 \theta_{v0} / \theta_{v0}} \equiv \sqrt{g/H_a} \quad (9)$$

is the Brunt–Väisälä frequency. Here and elsewhere,  $H_a$  represents the scale height of the atmosphere. The following shows that the condition  $\omega \gg N$  permits one to neglect  $S_b$  outside the storm.

First note that air parcels conserve  $\theta_v$  and  $r_v$  in the hydrometeor-free radiation zone ( $x \rightarrow \infty$ ). Assuming linearization is valid, conservation of  $\theta_v$  reduces to

$$\partial_t \theta'_v \approx -u_3 \partial_3 \theta_{v0} \quad x \rightarrow \infty. \quad (10)$$

Furthermore, Eq. (3) reduces to

$$\partial_t \Pi' \approx -\frac{c_0^2}{\rho_0 \theta_{v0}^2} \partial_i (\rho_0 \theta_{v0} u_i) \quad x \rightarrow \infty. \quad (11)$$

Equation (10) implies that  $S_b \sim (N^2 c_0^2 U / \theta_{v0} \omega) / \min(\lambda, H_a)$ , in which  $U$  and  $\lambda$  are the characteristic velocity and wavelength of the radiation field. Equation (11) implies that  $\partial_t \Pi' \sim (c_0^2 U \omega / \theta_{v0}) / \min(\lambda, H_a)$ . Therefore,  $S_b / \partial_t \Pi' \sim N^2 / \omega^2 \ll 1$  outside the storm.

The next issue concerns the importance of  $S_b$  as an acoustic source within the storm. On this matter, appendix A demonstrates that the infrasound of  $S_b$  is likely subdominant to the infrasound of  $S_m$ .

*f. The Coriolis source:  $S_c$*

Like  $S_b$ , the linear source term associated with the Coriolis force ( $S_c$ ) should be negligible. First consider the radiation zone. In general, one may write  $S_c = -(c_0^2 / \theta_{v0}) f \zeta_3$ . Using this relation and the partial time derivative of Eq. (11), one obtains  $S_c / \partial_t \Pi' \sim (f / \omega) (\zeta_3 / \partial_t u_i)$ . Here, it is assumed that  $\lambda \lesssim H_a$ . Since  $f / \omega \ll 1$  and acoustic waves are characterized by  $\zeta / \partial_t u_i \ll 1$ , the relation  $S_c / \partial_t \Pi' \ll 1$  is firmly satisfied outside the storm.

Within the storm, one may directly compare  $S_c$  with the classic vortex sound source. If the last two terms on the right-hand side of Eq. (8) are ignored, one has  $S_{uu} \rightarrow (c_0^2 / \theta_{v0}) \nabla \cdot \zeta \times \mathbf{u}$ . Similarly, one may write  $S_c = (c_0^2 / \theta_{v0}) \nabla \cdot f \hat{x}_3 \times \mathbf{u}$ . It follows that  $S_c / S_{uu} \sim f / \zeta$ , which is much less than unity for storm-scale flows.

*g. The subgrid turbulence source:  $S_{tb}$*

The parameterized influence of subgrid turbulence on the resolved fluid motion is questionable in any cloud model. As a consequence, the simulated infrasound is likely inaccurate if  $S_{tb}$  is the dominant source. Could this ever occur?

For heuristic purposes, suppose that the ambient atmosphere is approximately uniform and that the source flow is approximately nondivergent. With these simplifications, one obtains  $S_{tb} \approx -(c_0^2 / \theta_{v0}) \partial_{ij} \sigma_{ij}$  and  $S_{uu} \approx (c_0^2 / \theta_{v0}) \partial_{ij} (u_i u_j)$ , in which  $\partial_{ij} \equiv \partial_i \partial_j$ . It is therefore reasonable to assume that the acoustic radiation

generated by  $S_{tb}$  is negligible in comparison with that of  $S_{uu}$  if  $\sigma_{ij} / u_i u_j \ll 1$ . Above the surface layer, c-RAMS uses the formula  $\sigma_{ij} = K_m (\partial_j u_i + \partial_i u_j)$ , in which  $K_m$  is a variable mixing coefficient. With isotropic Smagorinsky closure,  $K_m \sim a^2 \delta^2 U / l$ , in which  $U$  and  $l$  are the characteristic wind speed and length scale of the source flow,  $a$  is a constant typically of order 0.1, and  $\delta$  is the grid spacing of the numerical model. Hence,  $\sigma_{ij} / (u_i u_j) \sim a^2 \delta^2 / l^2 \ll 1$  above the surface layer. On the upper boundary of the surface layer,  $\sigma_{ij} \sim U_*^2$ , in which  $U_*$  is the friction velocity. With the assumption of a neutral surface layer and a roughness length of a few centimeters, one has  $U_* \sim 0.1U$  and  $\sigma_{ij} / (u_i u_j) \sim U_*^2 / U^2 \ll 1$ . It is therefore expected that  $S_{tb}$  has only secondary importance.<sup>1</sup>

*h. Neglected sources in c-RAMS*

An additional source term,

$$S_{p\theta} \equiv \frac{c_0^2}{\rho_0 \theta_{v0}^2} \partial_i (\rho_0 \theta_{v0} \theta'_v \partial_i \Pi'), \quad (12)$$

would appear on the right-hand side of Eq. (6) without neglecting the acceleration due to  $-\theta'_v \partial_i \Pi'$  in the momentum equation. A scale analysis in appendix A suggests that  $S_{p\theta}$  may readily compete with  $S_{uu}$  in a turbulent cloud but is probably subdominant to  $S_m$  (cf. AG09). Although not directly simulated by c-RAMS, the infrasound of  $S_{p\theta}$  may be computed independently, if desired. Section 3 describes an adequate procedure.

Note that c-RAMS also neglects the acoustic radiation of electrical phenomena, which are not simulated by the model (Few et al. 1967; Dessler 1973; Georges 1976; Depasse 1994; Farges and Blanc 2010). It is reasonable to hypothesize that acoustic radiation associated with lightning could interfere with the infrasound of tornadoes or moist turbulence, even though its primary spectral peak appears to be in the low audio. However, Bedard (2005) reports no obvious connection between lightning events and the strong, sustained 0.5–5-Hz infrasound that seems to be a distinct feature of a tornadic storm.

**3. The Infrasonic Source Analysis Routine: ISAR**

The source terms in Eqs. (7) and (12) are readily computed from c-RAMS output. It is tempting to

<sup>1</sup> The subtle effect of surface shear stress on acoustic radiation has received considerable attention in the literature, and there are circumstances under which it may be significant (Shariff and Wang 2005; Hu et al. 2003; Howe 1979). However, a lengthy discussion on the topic is not required to understand the c-RAMS simulations in this paper.

compare these terms without further processing to see which one dominates. However, such a comparison would not necessarily provide accurate insight into the relative magnitudes of the acoustic radiation fields, which are integrals of their respective sources weighted by a spatiotemporal Green function. It is generally more informative to compare the radiation fields directly.

The numerical procedure developed for this task is referred to as the Infrasonic Source Analysis Routine (ISAR). ISAR consists of three basic steps:

- 1) filtering c-RAMS output (the source data),
- 2) computing the infrasound associated with individual source terms, and
- 3) comparing the individual infrasonic radiation fields.

Sections 3a and 3b briefly elaborate upon the workings of ISAR.

#### a. Filtering

The c-RAMS output contains atmospheric variables at discrete time intervals, which are smaller than the minimum wave period of interest. These variables are spatially staggered on an Arakawa C grid. The source terms are computed on the thermodynamic grid points, using low-order finite differencing in space and time.

The most rapid spatiotemporal variations of the acoustic source are usually removed with boxcar averaging. The smoothed source distribution is then multiplied by the weight functions  $W_t(t)$  and  $W_s(\mathbf{x})$ , in which  $\mathbf{x}$  is the position vector. Section 5b provides concrete examples of both. The temporal weight function  $W_t$  gradually introduces the acoustic source into the computational domain. The spatial weight function  $W_s$  is set to zero outside the source region that is under investigation to eliminate extraneous noise.

#### b. Computing and comparing the infrasonic radiation fields

The current manifestation of ISAR uses a relatively simple algorithm to compute the infrasound of a given source (or sum of sources)  $S_\alpha$ . The second-order AWE [Eq. (6) excluding unwanted sources] is split into the following two equations:

$$\begin{aligned} \partial_t \Pi'_\alpha &= \ddot{\Pi}'_\alpha \quad \text{and} \\ \partial_t \dot{\Pi}'_\alpha &= \frac{c_0^2}{\rho_0 \theta_{v0}^2} \partial_i (\rho_0 \theta_{v0}^2 \partial_t \Pi'_\alpha) + S_\alpha. \end{aligned} \quad (13)$$

Both  $\Pi'_\alpha$  and  $\dot{\Pi}'_\alpha$  are marched forward in time using a standard fourth-order Runge–Kutta scheme. Unless stated otherwise, the initial condition is  $\dot{\Pi}'_\alpha = \Pi'_\alpha = 0$ . So

as not to violate the acoustic Courant–Friedrichs–Lewy condition, the time steps are usually smaller than the sampling interval of c-RAMS data. A cubic interpolation function  $S_\alpha^c(t)$  is used for the source term  $S_\alpha(t)$  between sampling times  $t_i$  and  $t_{i+1}$ . The four coefficients of the cubic polynomial are obtained from the following matching conditions:  $S_\alpha^c = S_\alpha$  and  $\partial_t S_\alpha^c = \partial_t S_\alpha$  at both  $t_i$  and  $t_{i+1}$ .

The computation of  $\Pi'_\alpha$  generally employs two or more nested grids. Nesting significantly improves computational efficiency in the radiation zone, if the acoustic wavelength far exceeds the length scale of the source. As in c-RAMS, the grid spacing of each nested grid is uniform in the horizontal plane but can be stretched in the vertical direction. At the beginning of each time step, each parent grid and its daughter grid exchange boundary information near the lateral edges of the daughter grid.

The bottom boundary of the integration domain usually enforces the condition  $\partial_3 \Pi'_\alpha = 0$  and is reflective. By contrast, sponge layers absorb upward-propagating infrasound above the troposphere and outward-propagating infrasound beyond some user-defined radius. If desired, another sponge layer can be applied near the surface to damp downward-propagating waves.

The computational algorithm is parallelized in the Message Passing Interface paradigm for efficient use on a modern desktop workstation. The algorithm periodically saves  $\Pi'_\alpha$  onto a storage device. The stored values of  $\Pi'_\alpha$  correspond to time averages over the output interval. Separate runs can produce the infrasound of distinct sources. The radiation fields of all sources are then analyzed and compared using standard numerical methods. The most appropriate method varies, of course, with the peculiarities of the problem at hand.

## 4. Verification of ISAR and illustration of acoustic sources

The main purpose of this section is to demonstrate the validity of ISAR. To this end, it is shown that ISAR computations accurately reproduce the infrasound generated in two benchmark c-RAMS simulations. Both simulations illustrate fundamental mechanisms of infrasound production that have relevance in convective storm simulations. The first simulation involves the infrasound of adiabatic vortex fluctuations. The second involves the infrasound of evaporating cloud droplets, which exemplifies the infrasound of more general phase transitions.

#### a. Infrasound of a tornado-like vortex

A vortex fluctuation whose characteristic frequency  $\omega$  measurably exceeds the Brunt–Väisälä frequency  $N$  will

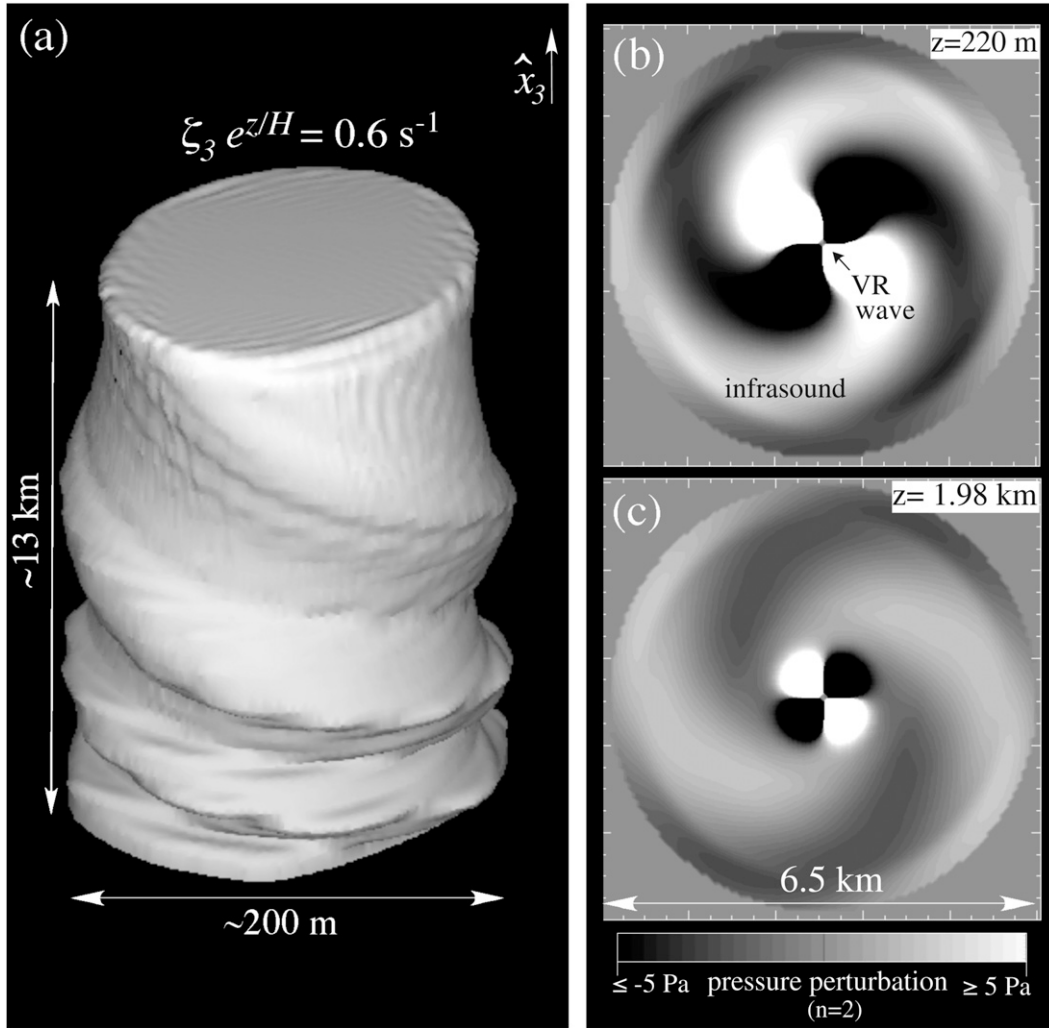


FIG. 1. A disturbed tornado and its infrasound. (a) The  $0.6 \text{ s}^{-1}$  isosurface of vertical vorticity  $\xi_3$  multiplied by  $e^{z/H}$ . The twisted elliptical deformation is due to a 3D VR wave. (b),(c) Horizontal slices of the wavenumber-2 pressure perturbation associated with the inner VR wave and outer infrasound. All plots are snapshots at  $t = 19.6 \text{ s}$ .

often (but not necessarily) emit acoustic radiation. In the parameter regime of a tornado, vortex Rossby (VR) waves commonly satisfy this condition and radiate infrasound. Figure 1 illustrates the asymmetric vorticity perturbation and infrasound associated with a three-dimensional VR wave in a tornado-like vortex. Details of the experimental setup are presented in section 3d of S08. A relatively concise description seems more fitting for our purposes. To facilitate the discussion, a cylindrical coordinate system is introduced in which  $r$  is the radius from the central axis of the vortex,  $\varphi$  is the azimuth, and  $z$  is the vertical distance from the surface.

To begin with, the basic state of the atmosphere is dry and isothermal. The initial ( $t = 0$ ) state of the “tornado” is characterized by a vertical vorticity distribution of the form

$$\xi_3 \approx \begin{cases} Z_0 e^{-z/H} & r < r_b \\ 0 & r > r_b \end{cases}, \quad (14)$$

in which  $Z_0 = 2 \text{ s}^{-1}$  and  $H = 6 \text{ km}$ . The boundary radius of the core is given by

$$r_b \approx R_0 + \epsilon \cos(2\varphi), \quad (15)$$

in which  $R_0 = 100 \text{ m}$  and  $\epsilon \ll R_0$ . The pressure and thermal variables ( $\Pi$  and  $\theta_v$ ) are adjusted to satisfy nonlinear balance conditions (S08). The maximum tangential wind speed occurs on the surface at  $r \approx R_0$ , and is given by  $U \approx Z_0 R_0 / 2 = 100 \text{ m s}^{-1}$ . Because the ambient sound speed is  $c_0 = 347.2 \text{ m s}^{-1}$ , the Mach number  $M \equiv U/c_0$  is approximately 0.3. The secondary circulation is initially zero and remains minimal for

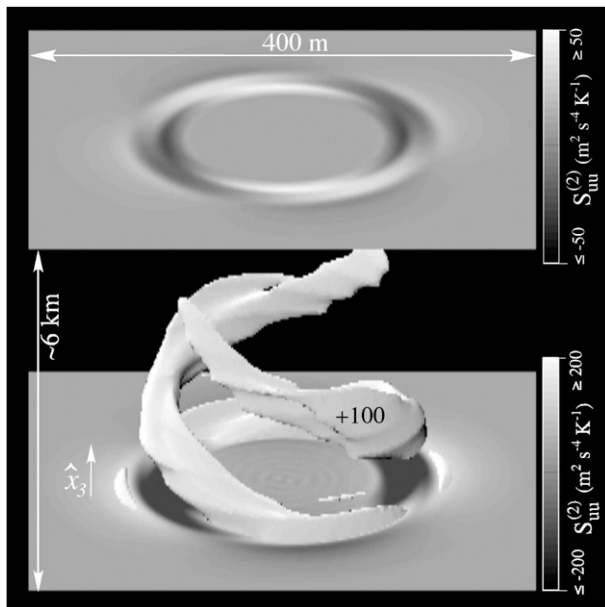


FIG. 2. A 3D visualization of the acoustic source term  $[S_{uu}^{(2)}]$  associated with the  $n = 2$  VR wave in Fig. 1. The contour plots are horizontal slices at  $z = 0.2$  km and  $z = 6.4$  km. The isosurface corresponds to  $S_{uu}^{(2)} = 100 \text{ m}^2 \text{ s}^{-4} \text{ K}^{-1}$ . The shading schemes of the contour plots and isosurface are unrelated.

the duration of the simulation (which has no surface drag).

The elliptical deformation of the vortex core [Eq. (15)] excites a three-dimensional VR wave with azimuthal wavenumber  $n = 2$ . The angular phase velocity of the VR wave decays with height, leading to a twisted elliptical core at later times. The vorticity perturbation associated with the VR wave (the  $n = 2$  component of  $\zeta$ ) is concentrated at the edge of the core. Over time, finite viscosity smooths the edge and slightly broadens the perturbation.

In theory, the VR wave generates infrasound through  $S_{uu}$  on the right-hand side of Eq. (6) (cf. Powell 1964; Howe 2003). To be precise, the primary acoustic source is the  $n = 2$  component (and its complex conjugate) of the following azimuthal Fourier expansion:

$$S_{uu} \equiv \sum_{n=-\infty}^{\infty} \hat{S}_{uu}^{(n)}(r, z, t) e^{in\phi}. \quad (16)$$

Figure 2 is a snapshot of  $S_{uu}^{(2)} \equiv 2\Re[S_{uu}^{(2)} e^{i2\phi}]$  at  $t = 19.6$  s. As expected, the acoustic source resides on the edge of the core, where the vorticity perturbation of the VR wave is maximal.

Figure 3 shows select time series of the infrasonic pressure perturbation  $p'$  that is generated by  $S_{uu}^{(2)}$  in the ISAR simulation (dotted curves). These recordings are taken 220 m above ground, at variable distances from the

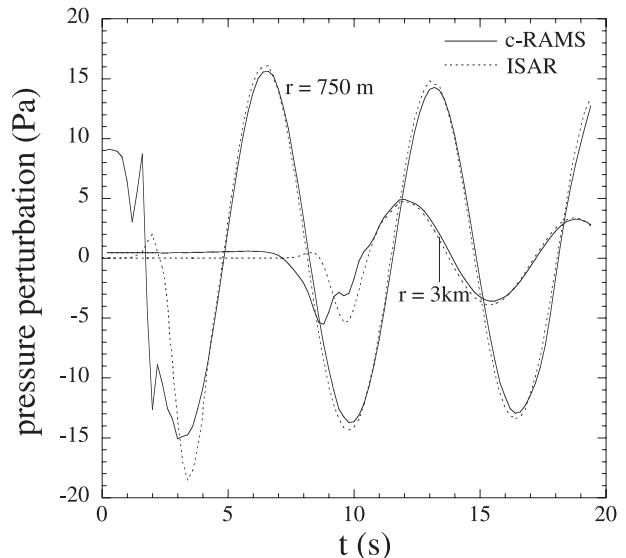


FIG. 3. Time series of the near-surface ( $z = 220$  m) infrasound generated by the  $n = 2$  VR wave in Fig. 1. The two measurements are made 750 m and 3 km from the center of the vortex. The solid and dotted curves correspond to c-RAMS and ISAR, respectively.

central axis of the vortex. The solid curves in Fig. 3 correspond to the  $n = 2$  component of  $p'$  in the c-RAMS simulation. After initial adjustment periods, which differ because of distinct initialization procedures, the ISAR and c-RAMS simulations agree.

#### b. Infrasound of an evaporating cloud of water droplets

As part of their effort to understand the fundamental thermoacoustics of c-RAMS, Schecter and Nicholls examined the infrasound generated by a spherical cloud of water droplets, suddenly introduced into an isentropic atmosphere at rest (SN10). In their study, vertical stratification was eliminated by neglecting gravity. The constant ambient values of  $p$  and  $\rho$  were  $10^5$  Pa and  $1.16 \text{ kg m}^{-3}$ , respectively. Experimental variables included the cloud radius  $R_c$ , the initial mean droplet size  $D_{m0}$ , the initial liquid mixing ratio  $r_{l0}$ , the relative humidity RH, and the constraints applied to the evolution of the droplet size distribution. Here, the case in which  $R_c = 200$  m,  $D_{m0} = 26 \text{ }\mu\text{m}$ ,  $r_{l0} = 0.46 \text{ g kg}^{-1}$ , and  $\text{RH} = 0$  is considered. In addition, the evaporation is governed by a single-moment microphysics parameterization that holds the number of droplets fixed.<sup>2</sup>

<sup>2</sup> The reader may consult Walko et al. (1995, 2000), Meyers et al. (1997), and Saleeby and Cotton (2004) for further information on this and more realistic microphysics parameterizations that are available in c-RAMS.

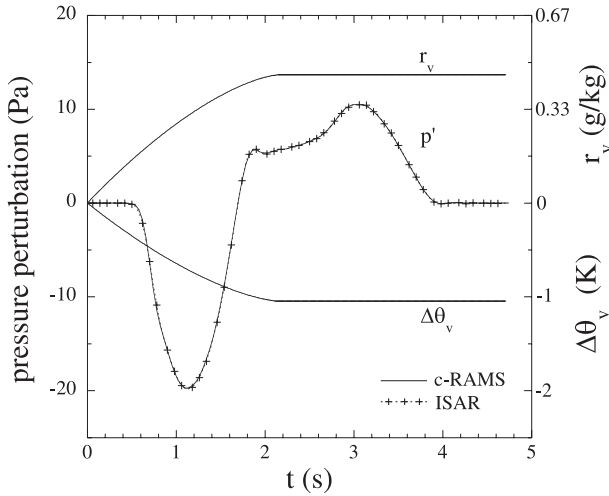


FIG. 4. Infrasound generated by cooling (and mass production) in an evaporating cloud of water droplets, suddenly introduced into a dry atmosphere at  $t = 0$ . The infrasonic pressure perturbation  $p'$  is measured 425 m from the center of the cloud, whereas the vapor mixing ratio  $r_v$  and the change of virtual potential temperature  $\Delta\theta_v$  are measured precisely on center. The three solid curves are from c-RAMS. The dotted curve with plus marks is the time series of  $p'$  that is reproduced by ISAR. The plus marks represent a fraction of the ISAR data points.

Figure 4 shows the cooling and growth of  $r_v$  that occur as the cloud evaporates. Both processes generate infrasound through  $S_m$  in Eq. (6), but the contribution from cooling tends to dominate (SN10). Figure 4 also compares the infrasonic pressure perturbation associated with  $S_m$  (according to ISAR) with that generated by c-RAMS. As in the vortex benchmark, good agreement between ISAR and c-RAMS is seen.

## 5. Demonstration of the utility of ISAR

### a. Numerically simulated infrasound of a towering cumulonimbus

Having illustrated the validity of ISAR, it is time to demonstrate its utility for uncovering the prevailing source of infrasound in a complex storm simulation. In this demonstration, an earlier c-RAMS simulation of a nonrotating, towering cumulonimbus is reexamined. The reader may consult section 4 of S08 for a detailed description of the experimental setup. By modern standards, the resolution of the simulation is relatively crude: the horizontal grid spacing is 30 m on the finest (inner) mesh, and the vertical grid spacing is continuously stretched from 5 to 74 to 464 m at altitudes of 5 m, 3 km, and 20 km, respectively. The simulation employs a single-moment microphysics parameterization, with seven discrete categories of ice, liquid, and mixed-phase hydrometeors. As

duly noted in S08, using c-RAMS with higher resolution (lower diffusivity) or one of its better microphysics parameterizations could very well alter the prevailing mechanism of infrasonic radiation. However, the provisional status of the simulation does not lessen its value for demonstrating the utility of ISAR.

The simulation begins with a warm bubble in a conditionally unstable atmosphere. The cumulonimbus fully develops in about 30 min. The airflow inside the cloud is fairly turbulent. In the vicinity of the melting layer, the maximum and root-mean-square wind speeds are approximately 35 and  $6.4 \text{ m s}^{-1}$ , respectively. Figures 5a–c show the ice, liquid, and total hydrometeor mixing ratios ( $r_{is}$ ,  $r_l$ , and  $r_{il}$ ) at the time  $t_0 \equiv 34.31 \text{ min}$ .<sup>3</sup> Figures 5d and 5e show the concurrent mixing ratios of hail and rain ( $r_h$  and  $r_r$ ). Note that the axis labels use the conventional notation ( $x, y, z$ ) for the Cartesian coordinates ( $x_1, x_2, x_3$ ).

Figure 5f is a snapshot (at  $t = 34.81 \text{ min}$ ) of the filtered pressure perturbation  $p'_f \equiv p' - \langle p' \rangle_{10s}$ , in which

$$\langle F \rangle_\tau \equiv \frac{1}{\tau} \int_{t-\tau/2}^{t+\tau/2} F(\tilde{t}) d\tilde{t} \quad (17)$$

for an arbitrary function of time  $F$ . In loose terms, the plot of  $p'_f$  shows all waves with frequencies at or above 0.1 Hz. In this frequency regime, the prevailing infrasound radiates from a compact region below the melting level, where hail transforms into rain. Furthermore, the characteristic wavelength is no less than a few hundred meters, meaning that the source has a characteristic frequency that is no greater than 1 Hz. ISAR may be used to answer the following question: Do phase transitions or local wind fluctuations generate this infrasound?

### b. Source filtering and controlling spurious initialization fronts

Step 1 of ISAR involves filtering the acoustic sources, which are computed from c-RAMS output every 0.2 s, over a 51-s time interval starting at  $t_0$ . For this study, the filtering is fairly basic. Temporal smoothing is applied to each source using 1.2-s boxcar averaging, so that  $S_\alpha \rightarrow \langle S_\alpha \rangle_{1.2s} \equiv \bar{S}_\alpha$ . This smoothing operation largely suppresses all spectral components of  $S_\alpha$  with frequencies that are greater than  $\sim 1 \text{ Hz}$ . With no loss of relevant information, the transformation  $\bar{S}_\alpha \rightarrow \bar{S}_\alpha - \bar{S}_{\alpha,A} \equiv \tilde{S}_\alpha$  is also made, in which  $A$  denotes the average of the subscripted variable over the entire observation window.

<sup>3</sup> Here the author has corrected Fig. 15 of S08, which used errant output generated by an earlier version of the standard RAMS postprocessing tool (“REVU”). The error pertained to the ice fraction of hail.

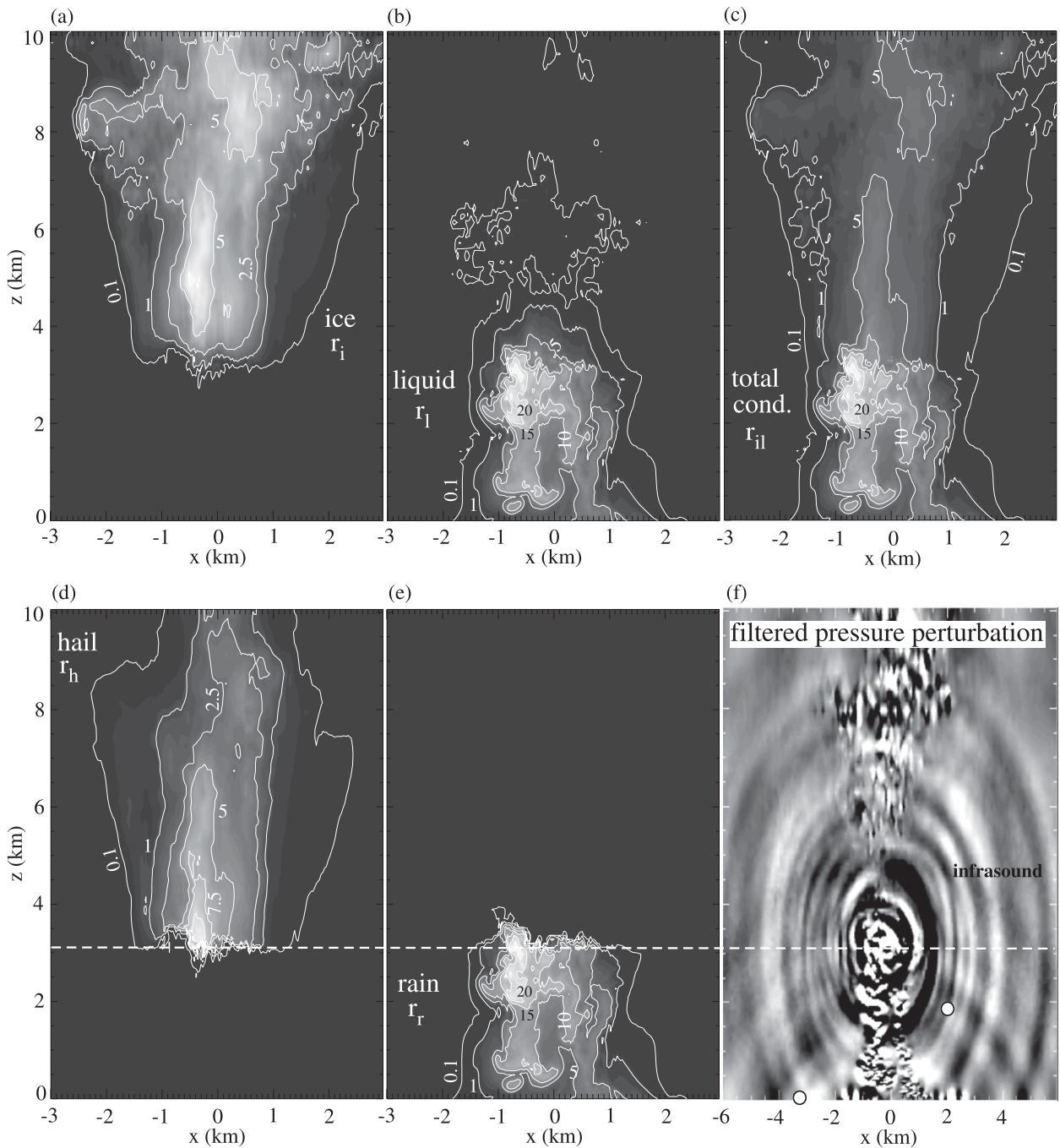


FIG. 5. Vertical slice through the center ( $y = 0$ ) of a numerically simulated cumulonimbus that emits relatively strong 0.1–1-Hz infrasound from a compact region below the melting level. (a)–(e) Mixing ratios (contours:  $\text{g kg}^{-1}$ ) of ice, liquid, total condensate, hail, and rain, respectively. Bright (dark) shades represent high (low) values, but the grayscale varies among the plots. (f) The filtered pressure perturbation  $p'_f$ , showing all waves with frequencies greater than about 0.1 Hz. The upper (white) and lower (black) extremes of the grayscale represent values of  $p'_f > 0.125$  and  $< -0.125$  Pa, respectively. The dashed line in the bottom row is roughly where hail changes into rain. The white circles in (f) are the observation points of the infrasonic time series that is shown later in Fig. 7.

Figure 6a is a plot of  $S_m^f \equiv \tilde{S}_m - \langle \tilde{S}_m \rangle_{10\text{s}}$ , which is essentially the 0.1–1-Hz frequency component of the acoustic source  $S_m$  that is directly associated with phase transitions of moisture. Clearly, it is located in the

same place as the origin of the infrasound. Figure 6b plots  $S_{uu}^f \equiv \tilde{S}_{uu} - \langle \tilde{S}_{uu} \rangle_{10\text{s}}$ , which is the 0.1–1-Hz frequency component of the acoustic source  $S_{uu}$  that is commonly associated with adiabatic turbulence or vortex fluctuations.

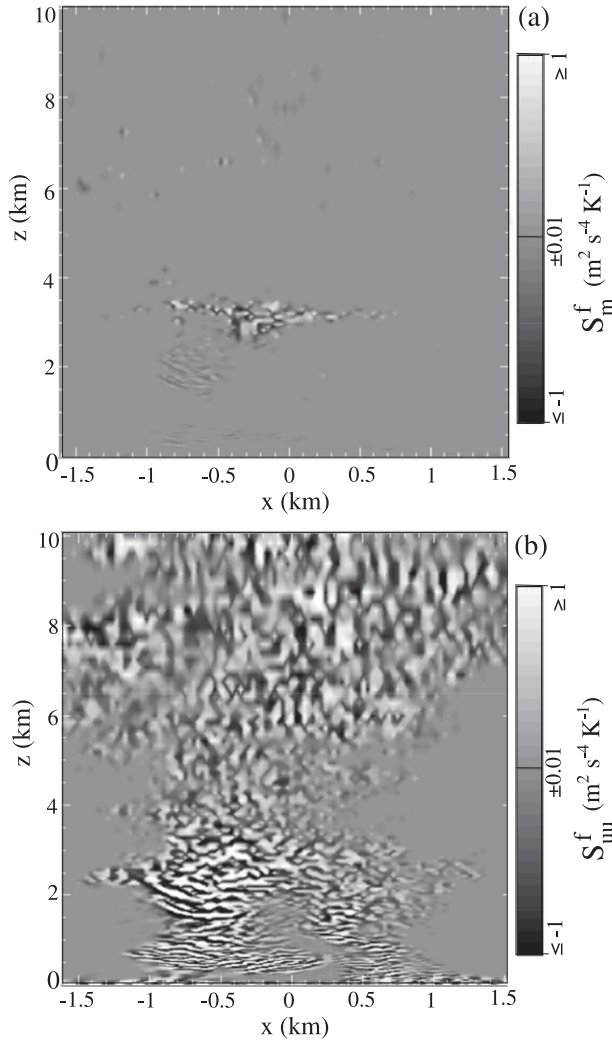


FIG. 6. Vertical slices (at  $y = 0$  and  $t' = 30$  s) of two sources of 0.1–1-Hz infrasound: (a) the acoustic source  $S_m^f$  associated with phase transitions of moisture and (b) the acoustic source  $S_{uu}^f$  associated with vortical turbulence. The positive and negative halves of the grayscales are logarithmic, and each covers two orders of magnitude. The absolute extremum of  $S_m^f$  in (a) is  $-3.2 \text{ m}^2 \text{ s}^{-4} \text{ K}^{-1}$ , whereas that of  $S_{uu}^f$  in (b) is  $-22.9 \text{ m}^2 \text{ s}^{-4} \text{ K}^{-1}$ .

Because  $S_{uu}^f$  is broadly distributed, it is reasonable to guess that it could not be the pertinent source of infrasound. On the other hand, the peak magnitude of  $S_{uu}^f$  (in the plotted vertical slice) exceeds that of  $S_m^f$  by a factor of 7. Therefore, a definitive conclusion requires comparison of the infrasonic radiation fields associated with both sources.

The infrasound of each source is computed after suddenly introducing that source into a resting atmosphere at  $t = t_0$ . Shocking the system in this way creates spurious pressure fronts (see appendix B). The infrasound at an arbitrary location becomes valid only after all fronts and their echoes have passed. It is desirable to minimize the

impact of spurious initialization fronts (SIFs) on the simulated infrasound. To reduce the intensity (steepness) of SIFs and their residual reflections from nested grid boundaries, the source distribution is gradually introduced over a finite (4 s) time interval  $\tau_r$ . Specifically,  $\tilde{S}_\alpha$  is multiplied by the following ramp function:

$$W_t(t') = \begin{cases} 0, & t' < 0 \\ 0.5\{1 + \sin[\pi(t'/\tau_r - 0.5)]\}, & 0 \leq t' \leq \tau_r, \\ 1, & t' > \tau_r \end{cases} \quad (18)$$

in which  $t' \equiv t - t_0$ . Furthermore, to eliminate SIFs from sources that are far outside the hail-to-rain transition zone,  $\tilde{S}_\alpha$  is multiplied by

$$W_s(\mathbf{x}) = \frac{1}{2} \left\{ 1 + \tanh \left[ \frac{10(R_s - |\mathbf{x} - \mathbf{x}_0|)}{R_s} \right] \right\}, \quad (19)$$

in which  $R_s = 1.5$  km and  $\mathbf{x}_0$  is near the center of the transition zone [ $(x_0, y_0, z_0) = (0, 0, 3)$  km]. The right-hand side of Eq. (19) is essentially a spherical step function that vanishes outside the radius  $|\mathbf{x} - \mathbf{x}_0| = R_s$ .

Section 5c examines the infrasound computed with ISAR at two locations, one on the ground and another aloft. For the latter case, undesirable surface echoes of SIFs are eliminated by imposing a linear sponge layer below  $z = 1.5$  km. The side effect of eliminating echoes of genuine infrasound is unimportant; at the elevated observation point, genuine echoes are substantially weaker than waves coming directly from the hail-to-rain transition zone.

c. Establishing the prevailing source

Figure 7 compares the infrasound of the cumulonimbus simulated with c-RAMS to the infrasound of  $S_m$  computed with ISAR. (To be precise, each ISAR result in Fig. 7 corresponds to the infrasound of  $\tilde{S}_\alpha W_t W_s$ .) The observation points reside 2.3 and 4.5 km from the center of the source region ( $\mathbf{x}_0$ ). The closer observation point is elevated, whereas the more distant one is on the ground (see Fig. 5f). The infrasonic recordings begin after all SIFs have passed (at  $t' = 20$  s). Each plotted time series is obtained with the following six-step postprocessing procedure:

- 1) The raw signal  $[p'(t')]$  is smoothed with 1.2-s boxcar averaging.
- 2) The linear trend of the smoothed signal is removed between  $t' = 20$  and 50 s.
- 3) The detrended signal is continued to  $t' = 80$  s by enforcing odd symmetry about  $t' = 50$  s.
- 4) The discrete Fourier transform of the continued (minute long) signal is computed.

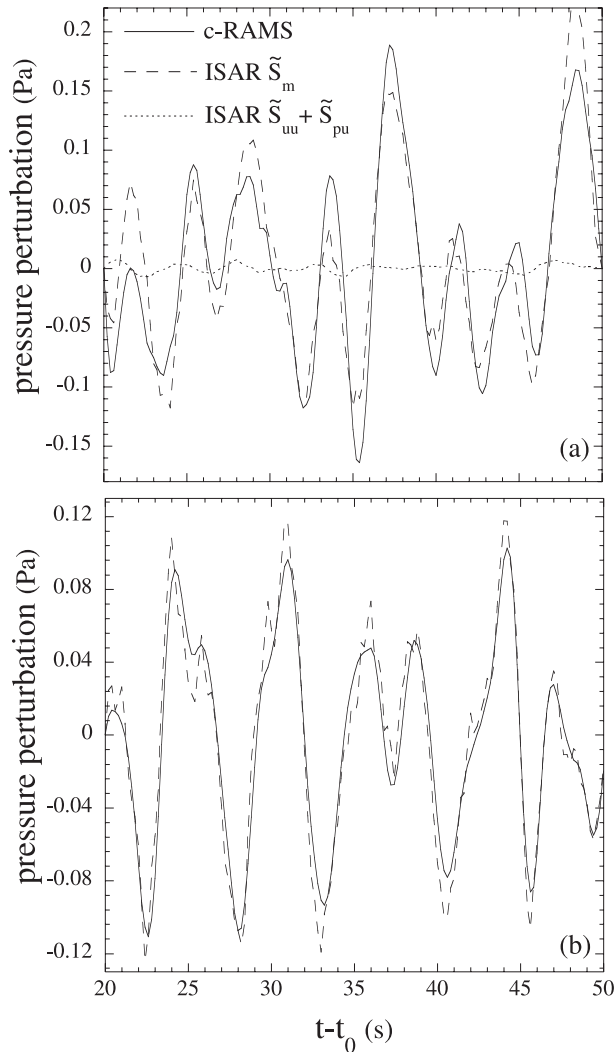


FIG. 7. Filtered time series of the infrasonic pressure perturbation generated by a numerically simulated towering cumulonimbus. The measurements are at (a)  $(x, y, z) = (2, 0, 1.85)$  km and (b)  $(x, y, z) = (-3.3, 0, 0)$  km. (See section 5c for a brief description of the signal processing.) The solid curves correspond to the total infrasound generated by c-RAMS. The dashed curves and dotted curve [in (a)] correspond to contributions from phase transitions of moisture and turbulent wind fluctuations, according to ISAR.

- 5) The Fourier transform is zeroed at frequencies  $< 0.1$  Hz.
- 6) The inverse of the revised Fourier transform (the filtered infrasound) is computed.

The filtered infrasound of  $S_m$  compares favorably to that of c-RAMS. Specifically, all major peaks of the  $S_m$  and c-RAMS signals occur simultaneously, and those that coincide have the same magnitudes. Therefore,  $S_m$  is the prevailing source of 0.1–1-Hz infrasound.

Having established the dominance of  $S_m$ , it is unnecessary to consider  $S_{uu}$ ,  $S_{pu}$ ,  $S_b$ ,  $S_c$ , or  $S_{tb}$ .

TABLE 1. Key parameters for the melting-hail experiment. First row (left–right): ambient atmospheric pressure, temperature, and sound speed. Second row: ambient vapor and saturation vapor mixing ratios. Third row: initial mixing ratio and liquid mass fraction of hail (within the spherical cloud). Fourth row: cloud radius, mean hail diameter, and mean rain diameter. Bottom row:  $\nu$  parameters for the size distributions of hail and rain.

Parameters	Values
$P_0, T_0, c_0$	711.73 hPa, 10.88°C, 338.7 m s <sup>-1</sup>
$r_{v0}, r_{v^*0}$	8.66, 11.6 g kg <sup>-1</sup>
$r_{h0}, \mu_{h0}$	10 g kg <sup>-1</sup> , 0
$R_c, D_{mh}, D_{mr}$	200 m, 1.4 mm, 0.55 mm
$\nu_h, \nu_r$	2, 1

Nevertheless, the dotted curve in Fig. 7a shows the computed infrasound of  $S_{uu} + S_{pu}$ , at the elevated observation point. As expected, the pressure fluctuations are relatively weak. This result is robust to changing  $W_s$  from a spherical weight function [Eq. (19)] to a slab weight function that is unity below 4.5 km and zero above. One might speculate that the infrasound of  $S_{p\theta}$  could have prevailed over that of  $S_m$ , if simulated by c-RAMS. However, the scale estimates of AG09 and appendix A do not support this hypothesis.

#### d. Physical or artificial?

ISAR has successfully verified that diabatic sources dominate the production of infrasound (with  $\omega \geq 0.1$  Hz) in the numerical simulation of a towering cumulonimbus. However, ISAR cannot tell us if these sources are realistically modeled in the acoustic parameter regime. Note that the infrasound is generated in a very narrow transition layer where hail becomes rain. As demonstrated below, the single-moment microphysics parameterization of c-RAMS has the potential to create spurious noise during the hail-to-rain category conversion.

Consider a c-RAMS simulation in which a spherical cloud of hail with a uniform mixing ratio  $r_{h0}$  is suspended in a homogeneous, resting atmosphere. Let the initial microphysics parameters and atmospheric conditions be similar to those in the hail-to-rain transition layer of the cumulonimbus experiment. Let us also use the same single-moment microphysics model, in which the probability distribution function of the hail or rain diameter  $D$  is given by

$$f_D = \frac{1}{\Gamma(\nu)} \left( \frac{\nu D}{D_m} \right)^{\nu-1} \frac{\nu}{D_m} e^{-\nu D/D_m}, \quad (20)$$

and the mean diameter  $D_m$  (as opposed to the number concentration) is fixed. Here,  $\Gamma$  is the standard gamma function of applied mathematics (e.g., Abramowitz and

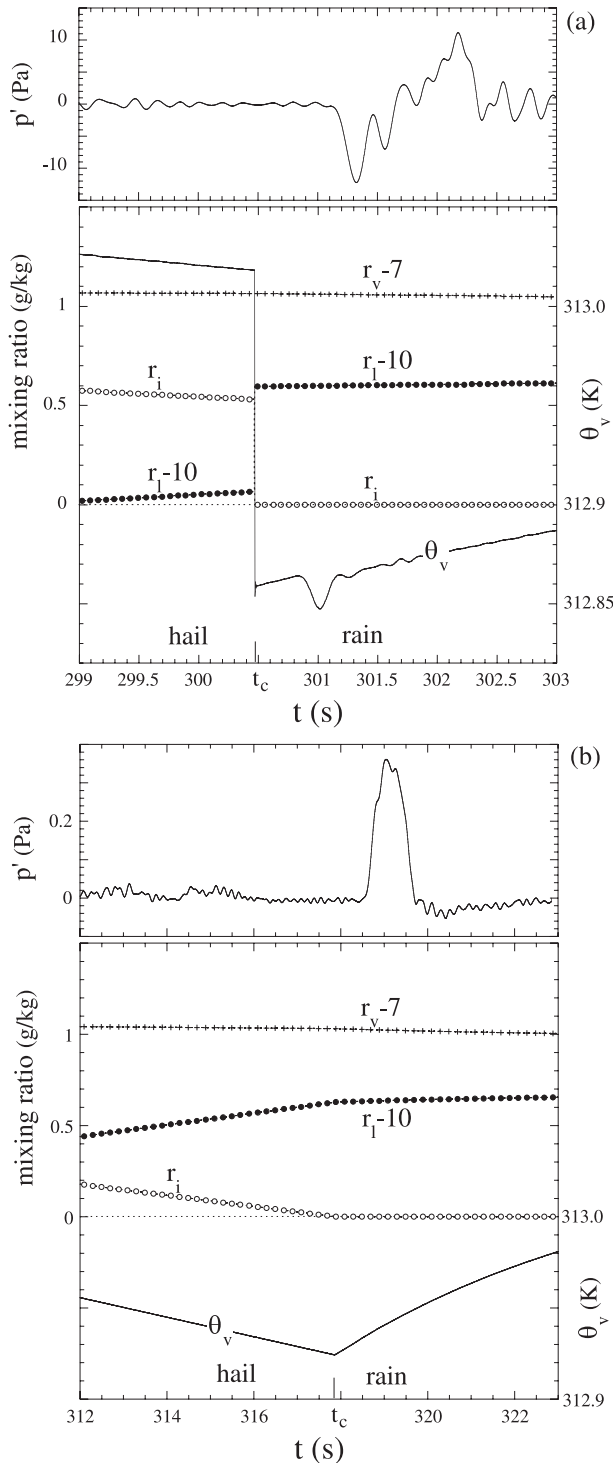


FIG. 8. Time series of select variables during category conversion from hail to rain in a spherical cloud, simulated with a single-moment (constant  $D_m$ ) microphysics parameterization in c-RAMS. The two graphs correspond to cases in which the conversion is triggered when the liquid mass fraction of hail passes (a)  $\mu_{lc} = 0.95$  and (b)  $\mu_{lc} = 0.9999$ . The pressure perturbation  $p'$  is measured at a distance of 0.45 km from the center of the cloud, whose radius is 0.2 km. The vapor, liquid, and ice mixing ratios ( $r_v$ ,  $r_l$ , and  $r_i$ ), as

Stegun 1972) and the value of  $\nu$  depends on the hydrometeor. The key parameters of the simulation are listed in Table 1. In addition, the terminal velocities of hail and rain are set to zero.

Because the atmospheric temperature is far above  $0^\circ\text{C}$ , the hail begins to melt. Figure 8a shows the time series of  $r_i$ ,  $r_l$ ,  $r_v$ , and  $\theta_v$  in the center of the cloud, near the time  $t_c$  when hail changes into rain. In this experiment, the transition occurs over a single time step of 2 ms, when the liquid mass fraction  $\mu_l$  of hail passes the critical value  $\mu_{lc} = 0.95$ . The transition involves a finite drop of  $r_i$  and a compensating jump of  $r_l$ . The latent heat required for this rapid melting event causes a discontinuous drop of  $\theta_v$ . Furthermore, the limiting values of  $\partial_t\theta_v$  before and after the transition are unequal. These artificial discontinuities create a false singularity in  $S_m$ . The top plot in Fig. 8a shows the infrasonic pressure perturbation ( $p'$  outside the cloud) associated with the singularity. The time scale of the acoustic emission is given by  $\tau_e = 2R_c/c_0$ , in which  $R_c$  is the cloud radius. The secondary oscillations are presumably due to slightly unsynchronized category transformations across the cloud.

Figure 8b is similar to Fig. 8a, but for  $\mu_{lc} = 0.9999$ . A seemingly minor change to the microphysics algorithm (the value of  $\mu_{lc}$ ) has profoundly reduced the  $\theta_v$  discontinuity and the associated acoustic emission. This result illustrates the need for caution when interpreting the acoustic emissions of a simulated storm, especially at high frequencies. For future simulations, increasing  $\mu_{lc}$  toward unity would seem prudent.

That being said, the acoustic defect under consideration may not be as harmful as the preceding, idealized experiment leads one to fear. During the review period of this paper, the author found that a towering cumulonimbus with  $\mu_{lc} = 0.9999$  emits approximately the same level of 0.1–1-Hz infrasound as the S08 storm, in which  $\mu_{lc} = 0.95$ . Standard microphysics parameterizations may have other ways to create artificial infrasound, but a comprehensive study of the subject must be deferred to a later time.

### 6. Conclusions

This paper presented a systematic method for identifying the prevailing sources of infrasound in numerical simulations of convective storms. Individual sources

← well as the virtual potential temperature  $\theta_v$ , are measured at the center of the cloud. Category conversion in (a) involves a discernible discontinuity of  $\theta_v$ , whereas category conversion in (b) merely involves a discontinuity of  $\partial_t\theta_v$ .

were formally defined by terms on the right-hand side of an exact AWE for the perturbation Exner function  $\Pi'$  [Eq. (6)]. For simplicity, this equation was derived under the assumption that the mean flow outside the storm is negligible. Should the need arise, one could readily derive an alternative equation that incorporates the ambient mean flow into the free-wave operator  $\mathcal{L}_{\text{fw}}$ .

As formulated here, the acoustic analogy involved the following distinct sources:

- $S_m$ —a source directly associated with phase transitions of moisture,
- $S_{uu}$ —a source associated with adiabatic vortex fluctuations and turbulence,
- $S_{pu}$ —a secondary source involving  $u_i \partial_i \Pi'$  and  $\Pi' \partial_i u_i$ ,
- $S_b$ —a secondary source involving the vertical buoyancy acceleration,
- $S_c$ —a secondary source due to the Coriolis force,
- $S_{\text{tb}}$ —a secondary source due to viscous stresses, and
- $S_{p\theta}$ —a seemingly secondary source due to  $\theta'_v \partial_i \Pi'$  in the momentum equation.

To qualify as a “source,” it was required only that  $S_\alpha$  become negligible relative to the individual components of  $\mathcal{L}_{\text{fw}}(\Pi')$  far outside the storm. Section 2 and appendix A explained why  $S_{pu}$ ,  $S_b$ ,  $S_c$ , and  $S_{\text{tb}}$  should be insignificant under normal circumstances. In cloud turbulence,  $S_{p\theta}$  may compete with  $S_{uu}$ , but  $S_m$  theoretically generates stronger infrasound than both (AG09). The infrasound of  $S_{uu}$  seems most important in connection with unsteady tornadoes (Georges 1976; S08), but its intensity in comparison with the infrasound of  $S_m$  in a tornadic thunderstorm is an unresolved issue.

To establish which source prevails in a complex storm simulation, a computational procedure called ISAR was developed (see sections 3 and 4). For illustrative purposes, ISAR was used to show that  $S_m$  was the prevailing source of 0.1–1-Hz infrasound in a c-RAMS simulation of a towering cumulonimbus (see section 5). Interestingly, direct comparison of  $S_{uu}$  and  $S_m$  did not suggest a clear winner. It proved necessary to compute and compare their radiation fields.

Of course, the prevailing source in a numerical simulation need not equate to the prevailing source in reality. In the cumulonimbus simulation considered here,  $S_m$  was concentrated in the hail-to-rain transition layer. This observation motivated a fundamental study of infrasound generated during the hail-to-rain category conversion in the single-moment microphysics model of c-RAMS. The study revealed that the conversion of hail into rain produces a false “singularity” in  $S_m$ . The spurious infrasound associated with this singularity may not have dominated the infrasound of the simulated

cumulonimbus, but its discovery underscored a need to further elucidate the acoustic peculiarities of parameterized microphysics. A thorough investigation into this matter could lead to refinements that are necessary for credible simulation results.

In conclusion, the acoustic analogy described above provides a useful framework for diagnosing the sources of infrasound in convective storm simulations. The prevailing source is found by carefully comparing the radiation fields of the primary candidates with a computational procedure such as ISAR. In general, further investigation is required to determine whether the prevailing source is created by physical or artificial means. Nevertheless, application of ISAR (or something similar) should play an important role in uncovering the dominant physical mechanisms that produce infrasound in future simulations of tornadic and nontornadic systems.

*Acknowledgments.* The author thanks Dr. Melville Nicholls, Dr. Alfred Bedard Jr., and Professor Roger Waxler for stimulating conversations on this research topic and two anonymous reviewers for their constructive comments. He also thanks Dr. Nicholls for providing the convective storm simulation data that were analyzed in section 5. This work was supported by NSF Grant AGS-0832320.

## APPENDIX A

### Scale Estimates of Several Acoustic Radiation Fields

#### *a. Far-field acoustic radiation of a compact source in a homogeneous unbounded atmosphere*

For the purpose of estimating the significance of a given source, it is useful to suppose that the unperturbed atmosphere is uniform. By doing so, the AWE governing the infrasound of  $S_\alpha$  simplifies to the following:

$$\partial_{ii} \Pi'_\alpha - c_0^2 \partial_{ii} \Pi'_\alpha = S_\alpha. \quad (\text{A1})$$

If one further assumes that the atmosphere is unbounded, the source is acoustically compact, and the observation point  $\mathbf{x}$  is many acoustic wavelengths from the source, the formal solution to Eq. (A1) is given by

$$\begin{aligned} \Pi'_\alpha(\mathbf{x}, t) &= \frac{1}{4\pi c_0^2} \int \frac{d^3 \mathbf{y}}{|\mathbf{x} - \mathbf{y}|} S_\alpha(\mathbf{y}, t - |\mathbf{x} - \mathbf{y}|/c_0) \\ &\approx \frac{1}{4\pi c_0^2 |\mathbf{x}|} \int d^3 \mathbf{y} S_\alpha(\mathbf{y}, t_*), \end{aligned} \quad (\text{A2})$$

in which the integral is over the source region and  $t_* \equiv t - |\mathbf{x}|/c_0 + \mathbf{x} \cdot \mathbf{y}/c_0|\mathbf{x}|$ . For a dipole source ( $S_\alpha \equiv \partial_i D_i$ ) or quadrupole source ( $S_\alpha \equiv \partial_{ij} Q_{ij}$ ), it is readily shown that

$$\Pi'_\alpha^{(\text{dipole})}(\mathbf{x}, t) \approx -\frac{x_i}{4\pi c_0^3 |\mathbf{x}|^2} \partial_t \int d^3 \mathbf{y} D_i(\mathbf{y}, t_*) \quad \text{or} \quad (\text{A3})$$

$$\Pi'_\alpha^{(\text{quad})}(\mathbf{x}, t) \approx \frac{x_i x_j}{4\pi c_0^4 |\mathbf{x}|^3} \partial_{tt} \int d^3 \mathbf{y} Q_{ij}(\mathbf{y}, t_*), \quad (\text{A4})$$

respectively (e.g., Howe 2003).

*b. Significance of infrasound generated by  $S_{pu}$*

Let us first examine the significance of the acoustic radiation field  $\Pi'_{pu}$  that is generated by  $S_{pu}$ . To begin with, one may conveniently rewrite  $S_{pu}$  as the following sum of (apparent) dipole and monopole sources:

$$S_{pu} = -\partial_t \left[ \partial_i (u_i \Pi') + \left( \frac{R}{c_v} - 1 \right) \Pi' \partial_i u_i \right]. \quad (\text{A5})$$

Applying Eqs. (A3) and (A2), one obtains

$$\begin{aligned} \Pi'_{pu}(\mathbf{x}, t) \approx & \frac{x_i}{4\pi c_0^3 |\mathbf{x}|^2} \partial_{tt} \int d^3 \mathbf{y} u_i \Pi'(\mathbf{y}, t_*) \\ & + \frac{1 - R/c_v}{4\pi |\mathbf{x}| c_0^2} \partial_t \int d^3 \mathbf{y} \Pi' \partial_i u_i(\mathbf{y}, t_*). \end{aligned} \quad (\text{A6})$$

Furthermore, one finds that

$$\begin{aligned} \Pi'_{uu}(\mathbf{x}, t) \approx & \frac{x_i x_j}{4\pi c_0^2 \theta_{v0} |\mathbf{x}|^3} \partial_{tt} \int d^3 \mathbf{y} u_i u_j(\mathbf{y}, t_*) \\ & + \frac{x_i}{4\pi c_0 \theta_{v0} |\mathbf{x}|^2} \partial_t \int d^3 \mathbf{y} u_i \partial_j u_j(\mathbf{y}, t_*) \quad \text{and} \quad (\text{A7}) \end{aligned}$$

$$\Pi'_m(\mathbf{x}, t) \approx \frac{1}{4\pi c_0^2 |\mathbf{x}|} \partial_t \int d^3 \mathbf{y} \frac{c^2}{\theta_v} \left( \frac{1}{\theta_v} \frac{d\theta_v}{dt} + \frac{1}{1 + r_v} \frac{dr_v}{dt} \right) (\mathbf{y}, t_*) \quad (\text{A8})$$

for the acoustic radiation fields of  $S_{uu}$  and  $S_m$ , respectively. Equations (A6)–(A8) can be used to assess the importance of  $S_{pu}$  in two classic paradigms.

The first paradigm under consideration is dry homeotropic turbulence at low Mach number (Lighthill 1952; Howe 2003). Here and throughout this subsection, the Coriolis force, gravity, and viscosity are neglected. The characteristic frequency of the turbulent motion is given by  $\omega \sim U/l$ , where  $U$  and  $l$  are the characteristic eddy velocity and eddy length scale, respectively. From the momentum equation, one obtains  $\Pi' \sim U^2/\theta_{v0}$  within the region of turbulent flow. Adiabatic thermodynamics

implies that  $\rho' \approx \rho_0 \theta_{v0} \Pi'/c_0^2$ . Applying this result to the mass continuity equation yields  $\partial_i u_i \sim M^2 U/l$ , in which  $M \equiv U/c_0$  is the Mach number of the turbulence. Accordingly, Eq. (A6) suggests that<sup>A1</sup>

$$\Pi'_{pu}^{(\text{HT})} \sim \frac{l}{4\pi |\mathbf{x}|} \frac{c_0^2}{\theta_{v0}} M^5 \max \left[ 1, M \left( 1 - \frac{R}{c_v} \right) \right]. \quad (\text{A9})$$

By comparison, Eq. (A7) suggests that

$$\Pi'_{uu}^{(\text{HT})} \sim \frac{l}{4\pi |\mathbf{x}|} \frac{c_0^2}{\theta_{v0}} M^4 \max(1, M). \quad (\text{A10})$$

Equations (A9) and (A10) imply that  $\Pi'_{pu}/\Pi'_{uu} \sim M \ll 1$ . In other words, the far-field acoustic radiation of  $S_{pu}$  is subdominant.

The second paradigm under consideration is an evaporating cloud of suspended water droplets in a resting atmosphere (SN10). If the thermoacoustics can be linearized, then the radiation field  $\Pi'_{pu}$  should be much less than  $\Pi'_m$  by virtue of its quadratic (as opposed to linear) dependence on the perturbation fields inside the cloud. The following shows that, under ordinary circumstances, linearization consistently yields  $\Pi'_{pu}/\Pi'_m \ll 1$ .

Let us start with the linearized momentum equation,  $\partial_i u_i = -\theta_{v0} \partial_i \Pi'$ , which implies that  $\Pi' \sim \omega l U/\theta_{v0}$ . Here we are concerned with the source region, where  $\omega$  is the evaporation rate,  $l$  is the cloud radius, and  $U$  is the velocity perturbation induced primarily by local cooling. Applying this estimate to Eq. (A6) yields

$$\Pi'_{pu}^{(\text{EC})} \sim \frac{l}{4\pi |\mathbf{x}|} \left( \frac{l}{\lambda} \right)^2 \frac{U^2}{\theta_{v0}} \max \left( \frac{l}{\lambda}, 1 - \frac{R}{c_v} \right), \quad (\text{A11})$$

in which (as usual)  $\lambda \equiv c_0/\omega$  is the acoustic wavelength.

To simplify the estimate of  $\Pi'_m$ , let us assume that cooling has a much larger impact than mass production (SN10) and keep only the component generated by  $d\theta_v/dt$ . In linear theory, one has  $\theta'_v \approx \theta_{v0}^2 \Pi'/c_0^2 - \theta_{v0} \rho'/\rho_0$ . Neglecting humidification in the mass continuity equation, one also has  $\partial_i \rho' \approx -\rho_0 \partial_i u_i$ . Using this approximation and the earlier estimate for  $\Pi'$  inside the cloud yields  $\theta'_v \sim \theta_{v0} (U/\omega l) \max[(l/\lambda)^2, 1]$ . Applying the preceding result for  $\theta'_v$  to the dominant term on the right-hand side of Eq. (A8), one obtains

$$\Pi'_m^{(\text{EC})} \sim \frac{l}{4\pi |\mathbf{x}|} \frac{l c_0 U}{\theta_{v0}} \max \left[ \left( \frac{l}{\lambda} \right)^2, 1 \right]. \quad (\text{A12})$$

<sup>A1</sup> For simplicity, it has been assumed that the volume occupied by the turbulence is of order  $l^3$ .

With the assumption that  $l/\lambda$  is of order unity or less, Eqs. (A11) and (A12) imply that the radiation fields satisfy  $\Pi'_{pu}/\Pi'_m \sim (l/\lambda)(U/c_0)$ . It is further estimated that  $U \sim \omega l \theta'_v / \theta_{v0} \sim \omega l L_{iv} r'_v / c_p T_0$ , in which  $L_{iv}$  is the latent heat of vaporization and  $T_0$  is the absolute temperature of the ambient atmosphere [cf. Eq. (7) of SN10]. Therefore,  $\Pi'_{pu}/\Pi'_m \sim (l/\lambda)^2 L_{iv} r'_v / c_p T_0$ . Under ordinary circumstances, the right-hand side of the preceding estimate is much less than unity.

### c. Significance of infrasound generated by $S_b$

Let us now see why the acoustic radiation field  $\Pi'_b$  of the buoyancy source  $S_b$  should be small relative to  $\Pi'_m$ . To begin with, Eq. (A3) implies that

$$\Pi'_b(\mathbf{x}, t) \approx \frac{g x_3}{4\pi c_0 \theta_{v0}^2 |\mathbf{x}|^2} \partial_t \int d^3 \mathbf{y} [\theta'_v - \theta_{v0}(r_t - r_v)](\mathbf{y}, t_*). \quad (\text{A13})$$

Neglecting the water-loading term in Eq. (A13), and the vapor mass production term in Eq. (A8), one obtains

$$\frac{\Pi'_b}{\Pi'_m} \sim \frac{g}{c_0 \omega}. \quad (\text{A14})$$

This suggests that the acoustic radiation generated by  $S_b$  is unimportant if  $\omega \gg g/c_0 \approx 0.03 \text{ s}^{-1}$ . Here, it has been tacitly assumed that the fluctuations of  $\theta_v$  are diabatically generated. If the Eulerian fluctuations are due solely to adiabatic stirring of preexisting entropy inhomogeneities in unsaturated air, then  $S_m = \Pi'_m = 0$ .

### d. Significance of infrasound generated by $S_{p\theta}$

Finally, let us consider the acoustic radiation  $\Pi'_{p\theta}$  of the source  $S_{p\theta}$  that is neglected in the current version of c-RAMS. With the usual approximations, Eq. (A3) implies that

$$\Pi'_{p\theta}(\mathbf{x}, t) \approx -\frac{x_i}{4\pi c_0 \theta_{v0} |\mathbf{x}|^2} \partial_t \int d^3 \mathbf{y} \theta'_v \partial_i \Pi'(\mathbf{y}, t_*). \quad (\text{A15})$$

For simplicity, suppose that turbulent motions (with characteristic velocity  $U$  and length scale  $l$ ) control the acoustic emission frequency, such that  $\omega \sim U/l$ . Further suppose that  $\Pi' \sim U^2/\theta_{v0}$  as in homentropic turbulence. Then, Eqs. (A15) and (A7) suggest that  $\Pi'_{p\theta}/\Pi'_{uu} \sim M^{-1}(\theta'_v/\theta_{v0})$ . Since  $M$  and  $\theta'_v/\theta_{v0}$  may be comparable in a turbulent cloud, this ratio is not necessarily small.

On the other hand,  $S_{p\theta}$  should be insignificant relative to  $S_m$  in the evaporating cloud paradigm. By analogy to the estimate of  $\Pi'^{\text{(EC)}}_{pu}/\Pi'^{\text{(EC)}}_m$  in Appendix A section b, one obtains  $\Pi'^{\text{(EC)}}_{p\theta}/\Pi'^{\text{(EC)}}_m \sim U/c_0 \sim (l/\lambda)L_{iv} r'_v / c_p T_0$ , which is generally much less than 1.

## APPENDIX B

### Controlling SIFs in ISAR

The method used by ISAR to control SIFs is best illustrated with a simple example. Consider a system of  $N_m$  point-monopole sources, each of the form

$$S_\alpha(\mathbf{x}, t) = A_\alpha \cos(2\pi t/\tau_\alpha) \delta(\mathbf{x} - \mathbf{x}_\alpha), \quad (\text{B1})$$

in which  $\delta$  is the 3D Dirac distribution. The amplitude  $A_\alpha$ , oscillation period  $\tau_\alpha$ , and position vector  $\mathbf{x}_\alpha$  are assumed to be independent of time. In an unbounded homogeneous atmosphere, the perturbation Exner function associated with the acoustic radiation field of the point-monopole system is given by

$$\Pi'(\mathbf{x}, t) = \frac{1}{4\pi c_0^2} \sum_{\alpha=1}^{N_m} \frac{A_\alpha}{r_\alpha} \cos(2\pi t_\alpha/\tau_\alpha), \quad (\text{B2})$$

in which  $r_\alpha \equiv |\mathbf{x} - \mathbf{x}_\alpha|$  and  $t_\alpha \equiv t - r_\alpha/c_0$ .

ISAR transforms  $S_\alpha$  into  $S_\alpha W_t$ , in which  $W_t$  is a temporal ramp function that is zero for  $t < t_0$ . Consequently, ISAR transforms  $\Pi'$  into

$$\Pi'^{\text{(ISAR)}}(\mathbf{x}, t) = \frac{1}{4\pi c_0^2} \sum_{\alpha=1}^{N_m} \frac{A_\alpha}{r_\alpha} \cos(2\pi t_\alpha/\tau_\alpha) W_t(t_\alpha). \quad (\text{B3})$$

Let  $N_m = 5$ ,  $\tau_\alpha = 10 \text{ s}$ ,  $c_0 = 340 \text{ m s}^{-1}$ , and  $r_\alpha = 250(\alpha + 1)$  in meters. Furthermore, let  $A_\alpha$  have the same arbitrary value for all  $\alpha$ . Figure B1 compares the actual  $\Pi'$  with  $\Pi'^{\text{(ISAR)}}$ , using Eq. (18) for  $W_t$ , with  $t_0 = 0$ . The three curves for  $\Pi'^{\text{(ISAR)}}$  correspond to ramping periods of  $\tau_r = 0.1, 1, \text{ and } 5 \text{ s}$ .

It is clear that eliminating source information for  $t < 0$  alters the frequency spectrum of the acoustic signal. The modification is manifest in the time series of the perturbation Exner function for  $t < t_1$ , in which  $t_1 = \tau_r + \max(r_\alpha/c_0)$ . If reflective surfaces exist, or partially reflective nested grid boundaries, then  $t_1$  increases because of echoes. If  $\tau_r$  is small, then the spurious fronts launched by each source at  $t = 0$  are relatively steep and easily discernible. Increasing  $\tau_r$  smooths each front and thereby damps the high-frequency (short wavelength) part of its spectral decomposition. Such damping can beneficially reduce partial reflections at nested grid boundaries (e.g., Koch and McQueen 1987). Eliminating SIFs from distant, secondary sources with a spatial filter  $W_s$  [such as that defined by Eq. (19)] would have the additional benefit of reducing  $t_1$ .

Note that point-monopole sources were considered for heuristic purposes. In reality, a localized source has

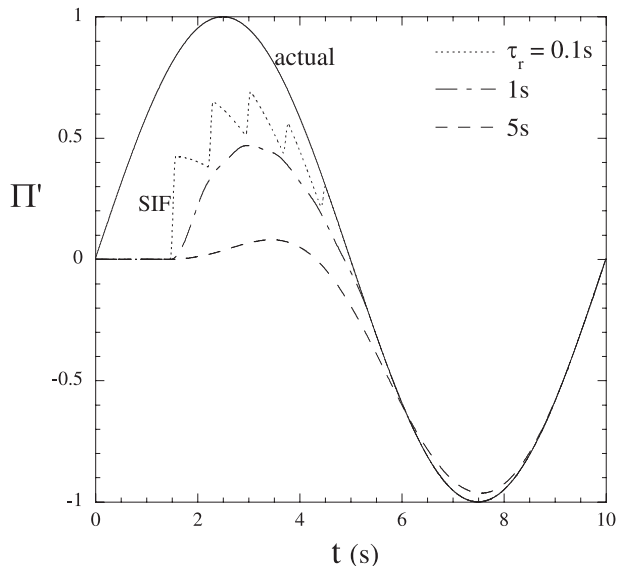


FIG. B1. The infrasonic emission generated by five point monopoles, observed 500 m from the nearest source. The units of the perturbation Exner function  $\Pi'$  are normalized to the peak value of the actual signal (solid curve), given by Eq. (B2). The dotted, dash-dotted, and dashed curves correspond to signals that would be generated by ISAR for ramping times  $\tau_r$ , equal to 0.1, 1, and 5 s.

a finite length scale  $l$ , and the SIF of its acoustic emission is smoothed over a time scale  $l/c_0$ .

#### REFERENCES

- Abramowitz, M., and A. Stegun, 1972: *Handbook of Mathematical Functions*. Dover, 1046 pp.
- Akhalkatsi, M., and G. Gogoberidze, 2009: Infrasonic generation by tornadic supercell storms. *Quart. J. Roy. Meteor. Soc.*, **135**, 935–940.
- , and —, 2011: Spectrum of infrasonic radiation from supercell storms. *Quart. J. Roy. Meteor. Soc.*, **137**, 229–235.
- Aurégan, Y., A. Maurel, V. Pagneux, and J.-F. Pinton, Eds., 2002: *Sound–Flow Interactions*. Springer-Verlag, 286 pp.
- Bedard, A. J., Jr., 2005: Low-frequency atmospheric acoustic energy associated with vortices produced by thunderstorms. *Mon. Wea. Rev.*, **133**, 241–263.
- , and T. M. Georges, 2000: Atmospheric infrasound. *Phys. Today*, **53**, 32–37.
- , B. W. Bartram, A. N. Keane, D. C. Welsh, and R. T. Nishiyama, 2004: The Infrasound Network (ISNet): Background, design details, and display capability as an 88D adjunct tornado detection tool. Preprints, *22nd Conf. on Severe Local Storms*, Hyannis, MA, Amer. Meteor. Soc., 1.1. [Available online at <http://ams.confex.com/ams/pdfpapers/81656.pdf>.]
- Cotton, W. R., and Coauthors, 2003: RAMS 2001: Current status and future directions. *Meteor. Atmos. Phys.*, **82**, 5–29.
- Depasse, P., 1994: Lightning acoustic signatures. *J. Geophys. Res.*, **99**, 25 933–25 940.
- Dessler, A. J., 1973: Infrasonic thunder. *J. Geophys. Res.*, **78**, 1889–1896.
- Farges, T., and E. Blanc, 2010: Characteristics of infrasound from lightning and sprites near thunderstorm areas. *J. Geophys. Res.*, **115**, A00E31, doi:10.1029/2009JA014700.
- Few, A. A., A. J. Dessler, D. J. Latham, and M. Brook, 1967: A dominant 200 Hz peak in the acoustic spectrum of thunder. *J. Geophys. Res.*, **72**, 6149–6154.
- Georges, T. M., 1976: Infrasonic from convective storms. Part II: A critique of source candidates. NOAA Tech. Rep. ERL 380–WPL 49, 59 pp. [Available from the National Technical Information Service, 5285 Port Royal Rd., Springfield, VA 22161.]
- Goldstein, M. E., 1976: *Aeroacoustics*. McGraw-Hill, 305 pp.
- , 2003: A generalized acoustic analogy. *J. Fluid Mech.*, **488**, 315–333.
- Howe, M. S., 1979: The role of surface shear stress fluctuations in the generation of boundary layer noise. *J. Sound Vib.*, **65**, 159–164.
- , 2003: *Theory of Vortex Sound*. Cambridge University Press, 216 pp.
- Hu, Z., C. L. Morfey, and N. D. Sandham, 2003: Sound radiation in turbulent channel flows. *J. Fluid Mech.*, **475**, 269–302.
- Johnson, J. B., R. C. Aster, and P. R. Kyle, 2004: Volcanic eruptions observed with infrasound. *Geophys. Res. Lett.*, **31**, L14604, doi:10.1029/2004GL020020.
- Koch, S. E., and J. T. McQueen, 1987: A survey of nested grid techniques and their potential for use within the MASS weather prediction model. NASA Tech. Memo. 87808, 26 pp.
- Lighthill, M. J., 1952: On sound generated aerodynamically, I. General theory. *Proc. Roy. Soc. London*, **A211**, 564–587.
- , 1954: On sound generated aerodynamically, II. Turbulence as a source of sound. *Proc. Roy. Soc. London*, **A222**, 1–32.
- Meyers, M. P., R. L. Walko, J. Y. Harrington, and W. R. Cotton, 1997: New RAMS cloud microphysics parameterization. Part II: The two-moment scheme. *Atmos. Res.*, **45**, 3–39.
- Nicholls, M. E., and R. A. Pielke Sr., 1994a: Thermal compression waves I: Total energy transfer. *Quart. J. Roy. Meteor. Soc.*, **120**, 305–332.
- , and —, 1994b: Thermal compression waves II: Mass adjustment and vertical transfer of total energy. *Quart. J. Roy. Meteor. Soc.*, **120**, 333–359.
- , and —, 2000: Thermally induced compression waves and gravity waves generated by convective storms. *J. Atmos. Sci.*, **57**, 3251–3271.
- Passner, J. E., and J. M. Noble, 2006: Acoustic energy measured in severe storms during a field study in June 2003. Army Research Laboratory Tech. Rep. ARL-TR-3749, 34 pp.
- Powell, A., 1964: Theory of vortex sound. *J. Acoust. Soc. Amer.*, **36**, 177–195.
- Saleeby, S. M., and W. R. Cotton, 2004: A large-droplet mode and prognostic number concentration of cloud droplets in the Colorado State University Regional Atmospheric Modeling System (RAMS). Part I: Module descriptions and supercell test simulations. *J. Appl. Meteor.*, **43**, 182–195.
- Schecter, D. A., and M. E. Nicholls, 2010: Generation of infrasound by evaporating hydrometeors in a cloud model. *J. Appl. Meteor. Climatol.*, **49**, 664–675.
- , —, J. Persing, A. J. Bedard Jr., and R. A. Pielke Sr., 2008: Infrasonic emitted by tornado-like vortices: Basic theory and a numerical comparison to the acoustic radiation of a single-cell thunderstorm. *J. Atmos. Sci.*, **65**, 685–713.
- Shariff, K., and M. Wang, 2005: A numerical experiment to determine whether surface shear-stress fluctuations are a true sound source. *Phys. Fluids*, **17**, 1–11.

- Stein, R. F., 1967: Generation of acoustic and gravity waves by turbulence in an isothermal stratified atmosphere. *Sol. Phys.*, **2**, 385–432.
- Szoke, E. J., A. J. Bedard Jr., E. Thaler, and R. Glancy, 2004: A comparison of ISNet data with radar data for tornadic and potentially tornadic storms in northeast Colorado. Preprints, *22nd Conf. on Severe Local Storms*, Hyannis, MA, Amer. Meteor. Soc., 1.2. [Available online at <http://ams.confex.com/ams/pdfpapers/81466.pdf>.]
- Walko, R. L., W. R. Cotton, M. P. Meyers, and J. Y. Harrington, 1995: New RAMS cloud microphysics parameterization. Part 1: The single-moment scheme. *Atmos. Res.*, **38**, 29–62.
- , —, G. Feingold, and B. Stevens, 2000: Efficient computation of vapor and heat diffusion between hydrometeors in a numerical model. *Atmos. Res.*, **53**, 171–183.
- Waxler, R., and K. E. Gilbert, 2006: The radiation of atmospheric microbaroms by ocean waves. *J. Acoust. Soc. Amer.*, **119**, 2651–2664.